

Ultrathin Planar Cavity Metasurfaces

Hsiang-Chu Wang, Cheng Hung Chu, Pin Chieh Wu, Hui-Hsin Hsiao, Hui Jun Wu, Jia-Wern Chen, Wei Hou Lee, Yi-Chieh Lai, Yao-Wei Huang, Ming Lun Tseng, Shu-Wei Chang, and Din Ping Tsai*

An ultrathin planar cavity metasurface is proposed based on ultrathin film interference and its practicability for light manipulation in visible region is experimentally demonstrated. Phase of reflected light is modulated by finely adjusting the thickness of amorphous silicon (a-Si) by a few nanometers on an aluminum (Al) substrate via nontrivial phase shifts at the interfaces and interference of multireflections generated from the planar cavity. A phase shift of π , the basic requirement for two-level phase metasurface systems, can be accomplished with an 8 nm thick difference. For proof of concept, gradient metasurfaces for beam deflection, Fresnel zone plate metalens for light focusing, and metaholograms for image reconstruction are presented, demonstrating polarization-independent and broadband characteristics. This novel mechanism for phase modulation with ultrathin planar cavity provides diverse routes to construct advanced flat optical devices with versatile applications.

For most of traditional optical devices, the desired wavefront shaping or optical functionalities are accomplished by engineering the optical path of light beams through transparent media. As the phase changes are gradually accumulated along the optical path, these optical components are usually bulky and very challenging to be integrated to achieve device miniaturization, which is highly desirable for the development of flat optical system. Metasurfaces,^[1–6] the 2D classification of the metamaterials,^[7,8] have attracted enormous attentions due to their extraordinary functionalities in manipulating phase and amplitude of electromagnetic wave at a subwavelength resolution^[9–12] and have been utilized in various applications,^[13,14] such as beam focusing,^[15–19] polarization control,^[20–22] holographic imaging,^[23–26] spin-orbit interaction,^[27] and so on. In

general, metasurfaces consist of an array of pre-designed resonators with varying geometries (multiresonance^[28–30] and gap-plasmon^[2,31,32] metasurfaces) or structural orientations (Pancharatnam–Berry–based metasurfaces)^[33,34] to satisfy the phase requirement for reconstructing a new wavefront according to the desired functionalities. However, these (polarization-dependent) metasurface platforms (not only for the metallic cases but also for the dielectric ones)^[35] usually highly depend on the design of geometrical and structural parameters, leading to a complicated process for the optimization of each unit to achieve complete control over light properties.

Recently, strong interference effect in highly absorptive media is proposed

for realizing wide-angle spectral selective absorbers and light harvesting devices.^[36–46] These studies show that the strong nanocavity interference occurs within a stack of layers composed of ultrathin lossy materials and metallic substrates. By employing the high optical loss and additional phase shift at the interface between dielectric and metallic substrate, reflectivity spectra in visible region can be significantly tailored even though the thickness of lossy medium varies in few nanometers. However, they are not capable of achieving a 2π phase modulation, which is the basic phase requirement for most optical devices and thus restricts their applications. To further investigate the optical characterizations of three-layer structure, a system consisting of high-index materials (complex refractive-index \tilde{n}_2) sandwiched by two semiinfinite spaces, air ($n_1 = 1$) and a metallic substrate (complex refractive-index \tilde{n}_3) is introduced, as shown in **Figure 1a**. The amplitude of the reflected wave $\tilde{\tau}$ is obtained from the superposition of the partial reflected wave $\tilde{\tau}_0$ at first interface and the sum of multiple reflections after m roundtrips in the cavity $\tilde{\tau}_m$ ($\tilde{\tau} = \tilde{\tau}_0 + \sum_{m=1}^{\infty} \tilde{\tau}_m$). They can be separately expressed as fol-

lowing: $\tilde{\tau}_0 = \tilde{r}_{12}$, and $\tilde{\tau}_m = \tilde{t}_{12} (\tilde{r}_{23}\tilde{r}_{21})^{m-1} \tilde{r}_{23}\tilde{t}_{21} e^{i\frac{2\pi\tilde{n}_2}{\lambda_0}(2T)m}$ ($m = 1, 2, 3, \dots$), where $\tilde{r}_{ij} = \frac{\tilde{n}_i - \tilde{n}_j}{\tilde{n}_i + \tilde{n}_j}$, $\tilde{t}_{ij} = \frac{2 \times \tilde{n}_j}{\tilde{n}_i + \tilde{n}_j}$ (for $i, j = 1, 2, \text{ or } 3$),

and T is the thickness of cavity. The reflectance (R) and phase shift ($\Delta\Phi$) can therefore be expressed as $R = \|\tilde{\tau}\|^2 = \tilde{\tau} \times \tilde{\tau}^*$ and $\Delta\phi = \arg(\tilde{\tau}) + 2\phi_{\text{air}}$ (ϕ_{air} is the phase accumulation of light propagation from the cavity surface to the reference plane), respectively. **Figure 1b** shows a phasor diagram for the entire process of light interference in an ultrathin cavity. The high impedance

H.-C. Wang, Dr. C. H. Chu, Dr. P. C. Wu, Dr. H. J. Wu, Dr. Y.-W. Huang, Dr. M. L. Tseng, Prof. S.-W. Chang, Prof. D. P. Tsai
 Research Center for Applied Sciences
 Academia Sinica
 Taipei 11529, Taiwan
 E-mail: dptsai@sinica.edu.tw

Prof. H.-H. Hsiao
 Graduate Institute of Biomedical Optomechatronics
 Taipei Medical University
 Taipei 11031, Taiwan

H.-C. Wang, J.-W. Chen, W. H. Lee, Y.-C. Lai, Prof. D. P. Tsai
 Department of Physics
 National Taiwan University
 Taipei 10617, Taiwan



The ORCID identification number(s) for the author(s) of this article can be found under <https://doi.org/10.1002/smll.201703920>.

DOI: 10.1002/smll.201703920

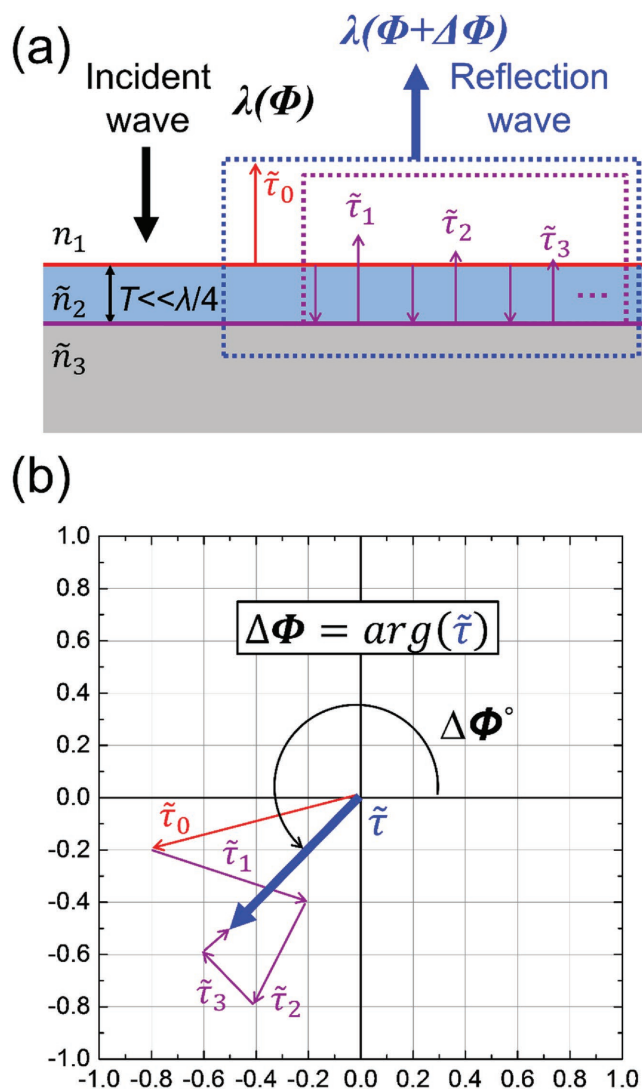


Figure 1. Light interference in a three-layer system. a) The reflected amplitude $\tilde{\tau}$ is the superposition from partial wave $\tilde{\tau}_0$ and multireflections ($\sum_{m=1}^{\infty} \tilde{\tau}_m$) out of the system. The strong multiple reflections in the ultrathin high-index film arise from high impedance mismatch at the front plane and high refractive metallic back plane. b) Phasor diagram of reflected light from the light interference of partial wave $\tilde{\tau}_0$ and multireflections ($\sum_{m=1}^{\infty} \tilde{\tau}_m$).

mismatch at the interface between the high-index materials and air as well as the interface between the high-index materials and reflective metallic substrate cause the strong multiple reflections of light within the high-index layers. Thus, arbitrary phases shift within 2π can be theoretically approached by adjusting the thickness T (partial reflection denoted by purple arrows in Figure 1). Based on the abovementioned discussions, it is evident that the ultrathin planar cavity offers an alternative way to straightforwardly modulate the phase of reflected light in the absence of complicated structural design.

In this paper, an ultrathin planar cavity metasurface comprising of amorphous silicon (a-Si) film radio frequency sputter (RF-sputter) deposited on aluminum (Al) substrate was

demonstrated for beam deflection, light focusing, and polarization-independent holographic imaging in visible spectrum. Such ultrathin planar cavity metasurfaces with film interference in a deeply subwavelength scale benefit from the advantages of broad operation bandwidth, ease of optimization, and high compatibility to Si industrial fabrication. This work paves a way for investigating the optical phenomena in high-index materials at an ultrathin spatial dimension and the development of flat optical components.

Figure 2a shows the numerical calculations of phase shift through an ultrathin a-Si film on Al substrate. The reflectivity spectra are also tailored with film thickness (see Figure S1 in the Supporting Information). One can observe that a 2π phase shift is achieved at a wide range of wavelength (from 550 to 850 nm) when the a-Si thickness is slightly adjusted. For example, the phase shift $\Delta\Phi$ covers the entire 2π range at the wavelength of 658 nm when T is adjusted from 15 to 50 nm (see Figure 2b). Details of optical characterizations for other

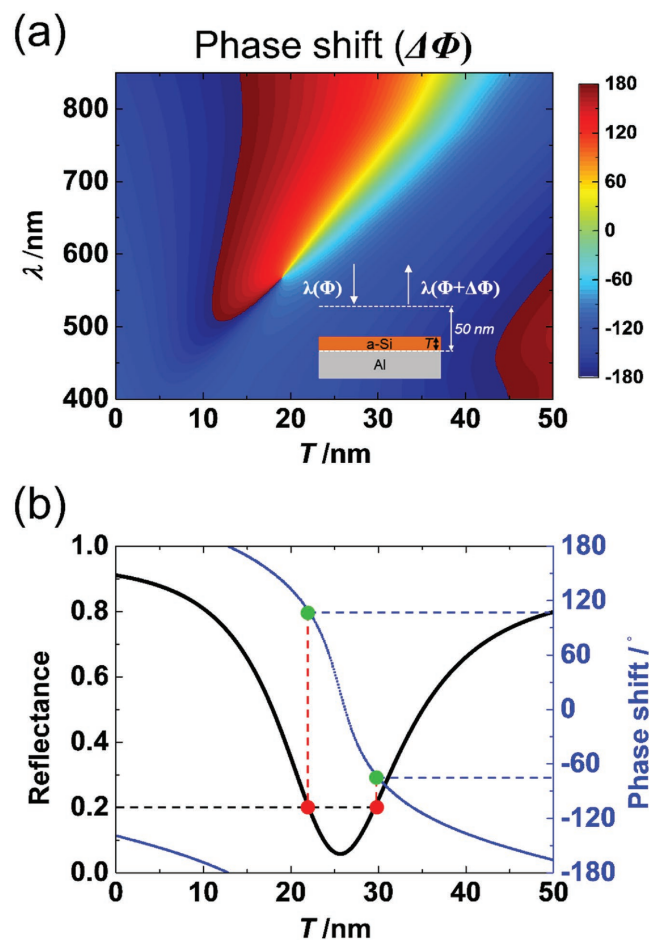


Figure 2. Phase shift of reflected light versus different a-Si film thickness (T) in visible spectrum. a) Color mapping for the phase shift as a function of thickness T of a-Si film and incident wavelength λ in free space. Inset shows the schematic representation of the film configuration and phase shift $\Delta\Phi$ from the interaction between light and thin film. b) Phase shift (blue line) and reflectance (black line) versus T at $\lambda = 658$ nm. The color symbols indicate the cavity thicknesses that are picked up for constructing the metasurfaces.

combinations of dielectrics and metallic substrate are shown in Figures S2 in the Supporting Information. Comparing to a general Fabry–Perot cavity in which the cavity length is at a scale of the effective optical wavelength, the proposed ultrathin planar cavity metasurface presents its capability on phase modulation at a deep subwavelength scheme. A two-level modulation is chosen to demonstrate the functionality of this system because of its unsophisticated design and fabrication. In general, two-level phase systems can obtain higher efficiency by increasing the reflectance or transmittance of each unit cell directly. Many works have utilized two-level system to demonstrate various devices, such as metahologram,^[25,46] tunable gradient metasurface,^[19] and focusing Fresnel zone plate (FZP).^[47] Here, we adopt two a-Si thicknesses as 22 and 30 nm (see color symbols in Figure 2b) to experimentally realize three metasurface devices: gradient metasurface, zone plate, and metahologram.

A two-level gradient metasurface device in the form of grating with duty cycle 50% is demonstrated. **Figure 3a** shows a corner of the fabricated device with structural period of 1 μm . To experimentally characterize the optical responses of fabricated gradient metasurface, we performed far-field measurements by an angular resolution optical system, which is illustrated in Figure S3a in the Supporting information. Based on the generalized Snell's law,^[1] the angle of reflection θ_r can be expected as $\theta_{r\pm} = \pm \sin^{-1}\left(\frac{\lambda}{P}\right)$ under normal illumination, where P is the periodicity of the supercell and the sign determines the incident and reflected lights locate at the right (+) or left (-) side related to the surface normal. **Figure 3b** shows the optical response of gradient metasurface with different periods changing from 0.6 to 2.0 μm at wavelength of 658 nm under normal incidence. The reflection mapping performs a symmetric profile because of the symmetry of structural configuration, while the specular reflection is almost suppressed. Different from the previously published papers of gradient metasurface, in which the anomalous reflected angles are discrete when the length of supercell is changed, this innovated approach is able to toward arbitrary reflected angles (changed in a smooth trend, see **Figure 3b**) without specular and higher order reflections due to the absence of limited size of unit cells. To examine isotropic responses of ultrathin planar cavity-based gradient metasurface, we measure the angle of reflection at different incident angles, while the period of gradient structure is fixed at $P = 1000$ nm (see **Figure 3c**). Theoretically, the reflected plane wave will take parallel wavevectors $k_x^{r+} = k_0 \sin \theta_i + \zeta$ and $k_x^{r-} = k_0 \sin \theta_i - \zeta$ from which the reflection angles θ_r can be derived as $\theta_{r+} = \sin^{-1}\left(\sin(\theta_i) + \frac{\lambda}{P}\right)$ and $\theta_{r-} = \sin^{-1}\left(\sin(\theta_i) - \frac{\lambda}{P}\right)$, where $\zeta = \partial\Phi/\partial P$ and k_0 is the wavevector of incident light. One can therefore expect that negative reflection occurs when the wavevector ζ is larger than $k_0 \sin \theta_i$ (i.e., $\frac{\lambda}{P} > \sin(\theta_i)$). Besides, the incident propagating wave can be converted into a surface wave when the incident angle is beyond the critical angle ($\theta_i > \theta_{\text{critical}} = \sin^{-1} \frac{\lambda}{P} = \sin^{-1} \frac{658}{1000} \cong 41^\circ$). One can also observe a similar phenomenon when the period is smaller than incident wavelength (for example, $P = 600$ nm).

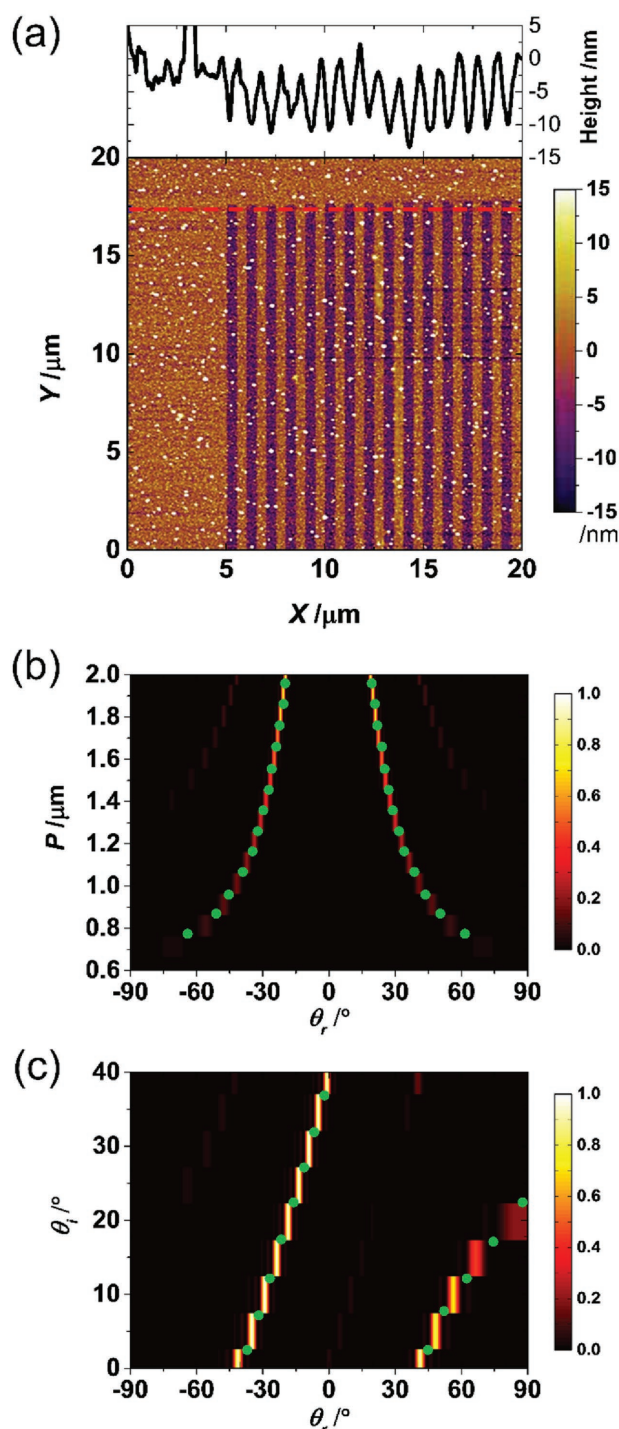


Figure 3. Far-field characterization from ultrathin two-level gradient metasurface at $\lambda = 658$ nm. a) AFM image of a corner of the $200 \mu\text{m} \times 200 \mu\text{m}$ sample with structural period (P) = 1000 nm. Top panel: cross-sectional profile along the red line at the bottom panel. b) Simulated far-field distribution (color map) and experimental measurement peaks (green circular marks) for b) various P and c) θ_i under a y -polarized illumination. The period of ultrathin two-level gradient metasurface is fixed at $P = 1000$ nm in panel (c).

Next, a two-level phase-based flat lens, FZP lens, was experimentally demonstrated in a reflection fashion. Spatial phase profile of a phase modulated flat lens follows the equation:

$\Phi(r) = \frac{2\pi}{\lambda}(\sqrt{r^2 + f^2} - f)$, where r is the distance from the lens center and f is the focal length. The designed FZP lens at $\lambda = 658$ nm with a diameter of 300 μm and 400 μm focal length ($\text{NA} \equiv n \times \sin \theta \approx 0.3511$ in air) is fabricated by standard e-beam lithography (EBL) processes. A scanning electron microscopy (SEM) image of the FZP lens is shown in Figure 4a. Since the phase modulation of our metalens only depends on the film thickness, the boundary of our FZP metalens is much smoother compared to those works that utilized scatterers in square or hexagonal unit cells to construct the required phase distributions. In addition, meta-FZPs (phase modulation) can be more promising than conventional FZPs (amplitude modulation) because the former can be much thinner with efficiency improved by increment of reflectance or transmittance of each unit cell. The performance of focusing is measured by the optical system, which is described in Figure S3b (Supporting Information). Figure 4b shows the experimental verification of the focusing spot size at the designed wavelength ($\lambda = 658$ nm). To clearly describe the focusing performance, intensity distribution of the focal spot is compared with a Gaussian profile. According to Figure 4c, the full width at half maximum of the focused spot size is about 2.7 μm ($\approx 4.1 \lambda$), which is very close to the theoretical value 2.3 μm ($1.22 \times \lambda/\text{NA}$). In addition to red light, the focusing ability of the designed lens is also exhibited for green light (532 nm) and blue light (470 nm) in Figure 4d,f, respectively with their corresponding intensity profile in Figure 4e,g. The broad operation band is the result of the combinations of phase and amplitude modulations.

Finally, we demonstrated a metahologram to reconstruct a desired image in visible region. The required phase distribution of metahologram is obtained by using computer-generated holograms method^[48] with iterative Fourier-transform algorithm at the optimized wavelength of 658 nm. For gray level holograms, the designed image (one bear for example) will be generated in each quadrant and zero-order beam at the origin. Considering two-level metaholograms, twin images will be accompanied with designed image (for more details, please refer to Figure S3c and in the Supporting Information). The metahologram consists of 200×200 pixels, each pixel made of $1.5 \mu\text{m} \times 1.5 \mu\text{m}$ unit cell with cavity thickness either 22 or 30 nm, the same as the ones used in the above devices. In fact, the pixel size can definitely be smaller than 1.5 μm . We have experimentally demonstrated the reflection angle strongly depends on the superlattice period of gradient metasurface as discussed above. When the period is shorter than incident wavelength λ , the reflection light would become surface wave without any reflection. Therefore, for an n -level phase modulation metasurfaces, the pixel size of each unit cell cannot be smaller than λ/n . In other words, the pixel size in our two-level metahologram cannot be smaller than half of wavelength. Figure 5a shows the high-contrast surface topography of the holographic sample measured by atomic force microscopy (AFM) with a desired reconstructed pattern in the inset. The simulated and experimental efficiency spectrum of this two-level metahologram is plotted in Figure 5b. The efficiency is defined as $E_{\text{image}} = W_{\text{out}}(\lambda)/W_{\text{in}}(\lambda)$, where $W_{\text{out}}(\lambda)$ and $W_{\text{in}}(\lambda)$ are the total power of images and the input laser power, respectively. Interestingly, the efficiency can be attributed to the combinations of phase and amplitude

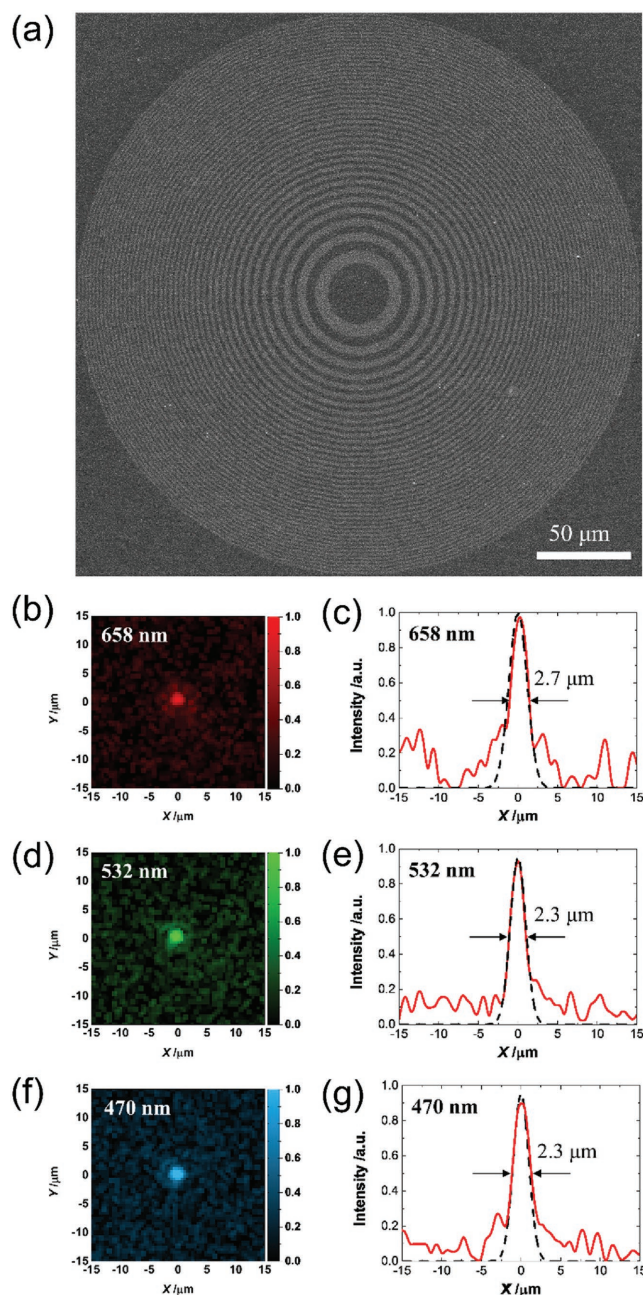


Figure 4. Focusing characterization of ultrathin planar cavity-based metalens. a) SEM image of an FZP lens with diameter 300 μm and focal length 400 μm ($\text{NA} \approx 0.3511$). b) Normalized intensity profile for red (658 nm) light on the focal plane and c) normalized light intensity profile along the focal spot. Corresponding analyses for d, e) green (532 nm) light and f, g) blue (470 nm) light.

modulation. For example, the reconstruction of the images at the wavelength of 658 nm mostly comes from phase modulation because a π -phase difference between two unit cells with comparable reflection intensities, while the operating mechanism at the wavelength of 532 nm results from both the phase modulation (30° phase difference) and amplitude modulation (32% reflectance difference). According to Figure 5c, the quantitative data for the phase and amplitude modulation curves

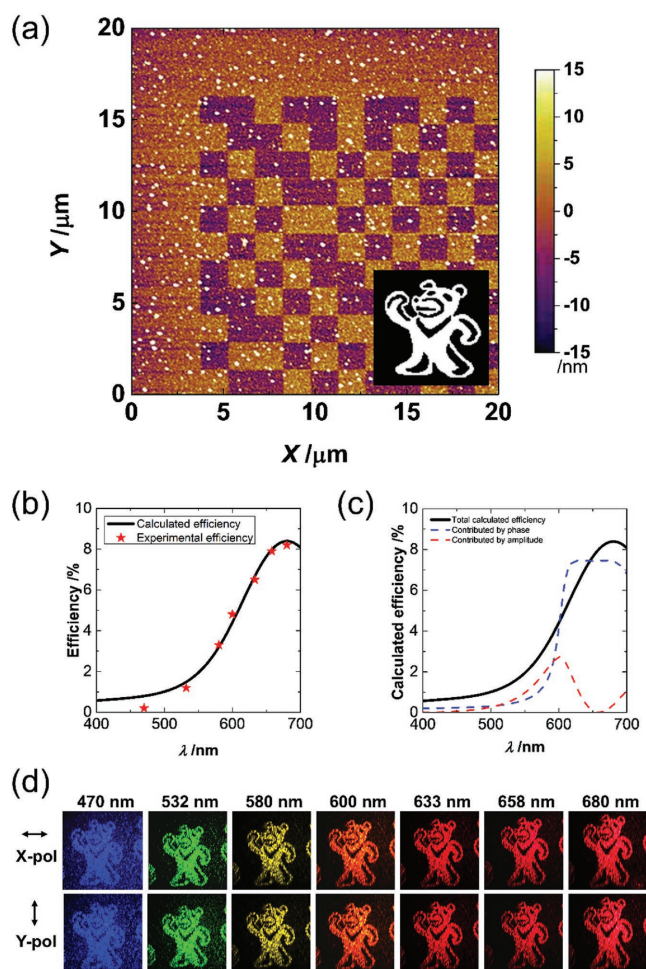


Figure 5. Ultrathin planar cavity metasurfaces for broadband metaholograms. a) AFM image of a corner of the $300\ \mu\text{m} \times 300\ \mu\text{m}$ metahologram sample with a desired pattern to be reconstructed in the inset. b) Experimental and calculated efficiency spectra of the metaholograms. c) Calculated efficiency spectra contributed individually from phase and amplitude. d) Reconstructed images under the illumination of an x - (top row) and y -polarized (bottom row) light with different wavelengths.

show great agreements with our speculation. The measured efficiency, which is marked by red star for each wavelength, shows that the designed metahologram with phase modulation exhibits the highest efficiency at the wavelength of 658 nm, which is the optimized condition from our design. The efficiency difference between simulated calculations and experimental measurements may result from the sample defects such as surface roughness and the variation in cavity thickness. In addition, the phase/amplitude modulation only depends on the thickness of a-Si, revealing the planar cavity metahologram is able to reconstruct the images with polarization-independence property. It can be verified by directly changing the orientation of the linearly polarized incident light. As shown in Figure 5d, the reconstructed images under x - and y -polarized illumination showing identical characteristics. Moreover, distinct images can be still observed in the wavelength range of 470–680 nm, performing a good agreement of the calculated efficiency shown in Figure 5b. These results well support that the ultrathin planar

cavity metahologram has the properties of broadband working range in visible spectrum and polarization independence.

In conclusion, we have demonstrated several optical devices based on ultrathin planar cavity metasurfaces, where the strong interference effect enables the phase modulation of reflection light by changing the cavity thickness in few nanometers at visible light. Due to the absence of anisotropic structures in unit cells, these fabricated metasurface devices for beam deflection, light focusing, and hologram exhibit the properties of polarization independence and broad working bandwidth. (For broad working bandwidth of beam deflection, please refer to Figure S5, Supporting Information.) The planar cavity metasurfaces are robust and tolerant in defects,^[49] which are more adoptive in practical applications. In addition, such planar cavity metasurfaces are also possible to be further applied to dynamically tunable devices by doping with proper impurities, which is a well-developed technology in current semiconductor process. Because the used material in our work is compatible to complementary metal oxide semiconductor fabrication process,^[50] which is a mature technology in multiple alignment by deep ultraviolet lithography, we can further achieve multiple order thickness control to improve the performance. Efficiency of this kind of metasurface can be enhanced by means of increasing the level of modulation or by optimizing the film structural designs, which are illustrated in Figures S6 and S7 (Supporting Information). This work paves versatile approaches to design robust, practical, and enduring metasurfaces.

Experimental Section

Fabrication of the sample was performed using a standard electron beam (e-beam) lithography, lift-off process, and reactive ion etching (RIE). 150 nm thick Al and 30 nm thick a-Si were orderly deposited on silicon substrate with e-beam evaporator and sputter, respectively. Positive photoresist (ZEP-520A) was used to define the thinner a-Si cavity and period in the EBL fabrication. RIE method was then used with CF_4 to etch 8 nm a-Si after e-beam lithography and developing process. $300\ \mu\text{m} \times 300\ \mu\text{m}$ samples were finished after removing the photoresist by immersing it in N,N -dimethylacetamide (ZDMAC) for about 5 min.

Supporting Information

Supporting Information is available from the Wiley Online Library or from the author.

Acknowledgements

The authors acknowledge financial support from Ministry of Science and Technology, Taiwan (Grant No. MOST-106-2745-M-002-003-ASP) and Academia Sinica (Grant No. AS-103-TP-A06). They are also grateful to National Center for Theoretical Sciences, NEMS Research Center of National Taiwan University, National Center for High-Performance Computing, Taiwan, and Research Center for Applied Sciences, Academia Sinica, Taiwan for their support.

Conflict of Interest

The authors declare no conflict of interest.

Keywords

beam deflection, Fresnel zone plates, metaholograms, metasurfaces, ultrathin planar cavities

Received: November 9, 2017

Revised: January 19, 2018

Published online: April 3, 2018

- [1] N. F. Yu, P. Genevet, M. A. Kats, F. Aieta, J. P. Tetienne, F. Capasso, Z. Gaburro, *Science* **2011**, 334, 333.
- [2] S. L. Sun, K. Y. Yang, C. M. Wang, T. K. Juan, W. T. Chen, C. Y. Liao, Q. He, S. Y. Xiao, W. T. Kung, G. Y. Guo, L. Zhou, D. P. Tsai, *Nano Lett.* **2012**, 12, 6223.
- [3] C.-F. Chen, C.-T. Ku, Y.-H. Tai, P.-K. Wei, H.-N. Lin, C.-B. Huang, *Nano Lett.* **2015**, 15, 2746.
- [4] L. Liu, X. Zhang, M. Kenney, X. Su, N. Xu, C. Ouyang, Y. Shi, J. Han, W. Zhang, S. Zhang, *Adv. Mater.* **2014**, 26, 5031.
- [5] M. Decker, I. Staude, M. Falkner, J. Dominguez, D. N. Neshev, I. Brener, T. Pertsch, Y. S. Kivshar, *Adv. Opt. Mater.* **2015**, 3, 813.
- [6] H.-H. Hsiao, C. H. Chu, D. P. Tsai, *Small Methods* **2017**, 1, 1600064.
- [7] Z. Kang, H. Zhang, H. Lu, J. Xu, H.-C. Ong, P. Shum, H.-P. Ho, *Opt. Lett.* **2012**, 37, 1748.
- [8] C. Aichen, F. Yangyang, X. Yadong, C. Huanyang, *J. Opt.* **2015**, 17, 105602.
- [9] K. E. Chong, I. Staude, A. James, J. Dominguez, S. Liu, S. Campione, G. S. Subramania, T. S. Luk, M. Decker, D. N. Neshev, I. Brener, Y. S. Kivshar, *Nano Lett.* **2015**, 15, 5369.
- [10] M. Q. Mehmood, S. Mei, S. Hussain, K. Huang, S. Y. Siew, L. Zhang, T. Zhang, X. Ling, H. Liu, J. Teng, A. Danner, S. Zhang, C.-W. Qiu, *Adv. Mater.* **2016**, 28, 2533.
- [11] K. Chen, Y. Feng, F. Monticone, J. Zhao, B. Zhu, T. Jiang, L. Zhang, Y. Kim, X. Ding, S. Zhang, A. Alù, C.-W. Qiu, *Adv. Mater.* **2017**, 29, 1606422.
- [12] M. L. Tseng, J. Yang, M. Semmlinger, C. Zhang, P. Nordlander, N. J. Halas, *Nano Lett.* **2017**, 17, 6034.
- [13] D. Fei, P. Anders, I. B. Sergey, *Rep. Prog. Phys.* **2018**, 81, 026401.
- [14] C. Hou-Tong, J. T. Antoinette, Y. Nanfang, *Rep. Prog. Phys.* **2016**, 79, 076401.
- [15] W. Zhu, Q. Song, L. Yan, W. Zhang, P.-C. Wu, L. K. Chin, H. Cai, D. P. Tsai, Z. X. Shen, T. W. Deng, S. K. Ting, Y. Gu, G. Q. Lo, D. L. Kwong, Z. C. Yang, R. Huang, A.-Q. Liu, N. Zheludev, *Adv. Mater.* **2015**, 27, 4739.
- [16] X. Chen, Y. Zhang, L. Huang, S. Zhang, *Adv. Opt. Mater.* **2014**, 2, 978.
- [17] X. Chen, L. Huang, H. Mühlenbernd, G. Li, B. Bai, Q. Tan, G. Jin, C.-W. Qiu, T. Zentgraf, S. Zhang, *Adv. Opt. Mater.* **2013**, 1, 517.
- [18] C. H. Chu, M. L. Tseng, J. Chen, P. C. Wu, Y.-H. Chen, H.-C. Wang, T.-Y. Chen, W. T. Hsieh, H. J. Wu, G. Sun, D. P. Tsai, *Laser Photonics Rev.* **2016**, 10, 986.
- [19] Y. W. Huang, H. W. H. Lee, R. Sokhoyan, R. A. Pala, K. Thyagarajan, S. Han, D. P. Tsai, H. A. Atwater, *Nano Lett.* **2016**, 16, 5319.
- [20] P. C. Wu, W. Zhu, Z. X. Shen, P. H. J. Chong, W. Ser, D. P. Tsai, A.-Q. Liu, *Adv. Opt. Mater.* **2017**, 5, 1600938.
- [21] P. C. Wu, W.-Y. Tsai, W. T. Chen, Y.-W. Huang, T.-Y. Chen, J.-W. Chen, C. Y. Liao, C. H. Chu, G. Sun, D. P. Tsai, *Nano Lett.* **2017**, 17, 445.
- [22] V. V. Klimov, I. V. Zabkov, A. A. Pavlov, R. C. Shiu, H. C. Chan, G. Y. Guo, *Opt. Express* **2016**, 24, 6172.
- [23] K. Huang, Z. G. Dong, S. T. Mei, L. Zhang, Y. J. Liu, H. Liu, H. B. Zhu, J. H. Teng, B. Luk'yanchuk, J. K. W. Yang, C. W. Qiu, *Laser Photonics Rev.* **2016**, 10, 500.
- [24] W. T. Chen, K. Y. Yang, C. M. Wang, Y. W. Huang, G. Sun, I. D. Chiang, C. Y. Liao, W. L. Hsu, H. T. Lin, S. Sun, L. Zhou, A. Q. Liu, D. P. Tsai, *Nano Lett.* **2014**, 14, 225.
- [25] Y. W. Huang, W. T. Chen, W. Y. Tsai, P. C. Wu, C. M. Wang, G. Sun, D. P. Tsai, *Nano Lett.* **2015**, 15, 3122.
- [26] G. Rui, Y. Ma, B. Gu, Q. Zhan, Y. Cui, *Opt. Lett.* **2016**, 41, 4379.
- [27] D. O'Connor, P. Ginzburg, F. J. Rodríguez-Fortuño, G. A. Wurtz, A. V. Zayats, *Nat. Commun.* **2014**, 5, 5327.
- [28] N. Yu, F. Aieta, P. Genevet, M. A. Kats, Z. Gaburro, F. Capasso, *Nano Lett.* **2012**, 12, 6328.
- [29] X. Ni, N. K. Emani, A. V. Kildishev, A. Boltasseva, V. M. Shalaev, *Science* **2012**, 335, 427.
- [30] O. Lecarme, Q. Sun, K. Ueno, H. Misawa, *ACS Photonics* **2014**, 1, 538.
- [31] A. Pors, S. I. Bozhevolnyi, *Opt. Express* **2013**, 21, 27438.
- [32] A. Pors, O. Albrektsen, I. P. Radko, S. I. Bozhevolnyi, *Sci. Rep.* **2013**, 3, 2155.
- [33] L. Huang, X. Chen, H. Mühlenbernd, G. Li, B. Bai, Q. Tan, G. Jin, T. Zentgraf, S. Zhang, *Nano Lett.* **2012**, 12, 5750.
- [34] S.-C. Jiang, X. Xiong, Y.-S. Hu, S.-W. Jiang, Y.-H. Hu, D.-H. Xu, R.-W. Peng, M. Wang, *Phys. Rev. B* **2015**, 91, 125421.
- [35] S. Jahani, Z. Jacob, *Nat. Nanotechnol.* **2016**, 11, 23.
- [36] M. A. Kats, R. Blanchard, P. Genevet, F. Capasso, *Nat. Mater.* **2013**, 12, 20.
- [37] H. M. Song, L. Q. Guo, Z. J. Liu, K. Liu, X. Zeng, D. X. Ji, N. Zhang, H. F. Hu, S. H. Jiang, Q. Q. Gan, *Adv. Mater.* **2014**, 26, 2737.
- [38] F. F. Schlich, R. Spolenak, *Appl. Phys. Lett.* **2013**, 103, 213112.
- [39] S. S. Mirshafieyan, J. P. Guo, *Opt. Express* **2014**, 22, 31545.
- [40] J. Park, J. H. Kang, A. P. Vasudev, D. T. Schoen, H. Kim, E. Hasman, M. L. Brongersma, *ACS Photonics* **2014**, 1, 812.
- [41] D. Liu, H. T. Yu, Z. Yang, Y. Y. Duan, *Nano Res.* **2016**, 9, 2354.
- [42] H. Dotan, O. Kfir, E. Sharlin, O. Blank, M. Gross, I. Dumchin, G. Ankonina, A. Rothschild, *Nat. Mater.* **2013**, 12, 158.
- [43] C. Rios, P. Hosseini, R. A. Taylor, H. Bhaskaran, *Adv. Mater.* **2016**, 28, 4720.
- [44] K. T. Lee, S. Seo, J. Y. Lee, L. J. Guo, *Adv. Mater.* **2014**, 26, 6324.
- [45] P. Hosseini, C. D. Wright, H. Bhaskaran, *Nature* **2014**, 511, 206.
- [46] Z. Yue, G. Xue, J. Liu, Y. Wang, M. Gu, *Nat. Commun.* **2017**, 8, 15354.
- [47] Q. Wang, E. T. F. Rogers, B. Gholipour, C.-M. Wang, G. Yuan, J. Teng, N. I. Zheludev, *Nat. Photonics* **2016**, 10, 60.
- [48] F. Wyrowski, O. Bryngdahl, *J. Opt. Soc. Am. A* **1988**, 5, 1058.
- [49] M. A. Kats, F. Capasso, *Appl. Phys. Lett.* **2014**, 105, 131108.
- [50] X. Wang, W. Shi, H. Yun, S. Grist, N. A. F. Jaeger, L. Chrostowski, *Opt. Express* **2012**, 20, 15547.